Tomographic SAR imaging with large elevation aperture a P-band small UAV demonstration

Zeng, Tao; Liu, Minkun; Wang, Yan; Ding, Zegang; Li, Linghao; Wang, Zhen; Wei, Yangkai; Wang, Jianping

DOI
10.1007/s11432-021-3391-2

Publication date
2022

Document Version
Final published version

Published in
Science China Information Sciences

SCIENCE CHINA
Information Sciences

• RESEARCH PAPER •

March 2022, Vol. 65 132303:1–132303:14
https://doi.org/10.1007/s11432-021-3391-2

Tomographic SAR imaging with large elevation aperture: a P-band small UAV demonstration

Tao ZENG[1,2,3], Minkun LIU[1,2], Yan WANG[1,2,3*], Zegang DING[1,2,3], Linghao LI[1,2], Zhen WANG[1,2], Yangkai WEI[1,2] & Jianping WANG[4]

[1]*Radar Research Lab, School of Information and Electronics, Beijing Institute of Technology, Beijing* 100081*, China;*
[2]*Beijing Institute of Technology Chongqing Innovation Center, Chongqing* 401120*, China;*
[3]*Yangtze Delta Region Academy of Beijing Institute of Technology, Jiaxing* 314019*, China;*
[4]*Faculty of Electrical Engineering, Mathematics and Computer Science* (*EEMCS*)*, Delft University of Technology, Delft* 2628CD*, Netherlands*

Received 27 August 2021/Revised 15 November 2021/Accepted 14 December 2021/Published online 14 February 2022

Abstract Elevation resolution is an important indicator in tomographic SAR imaging as it represents the ability to discriminate closed targets in elevation. In general, the elevation resolution is proportional to the length of the elevation aperture. However, as the elevation aperture increases, the geometric consistency of the image will undesirably deteriorate and hence fails the image coregistration approach required by the traditional super-resolution tomographic imaging. In this paper, a new super-resolution tomographic imaging method is proposed to overcome the inconsistency problem caused by the large elevation aperture. The core strategy is to get rid of two-dimensional image coregistration by applying a three-dimensional (3D) back projection like imaging manner: the 3D space is firstly divided into a 3D imaging grid, each of which is individually imaged via compressive sensing for super-resolution. The effectiveness of the proposed approach is evaluated by both computer simulations and real P-band UAV SAR data.

Keywords UAV SAR tomography, large elevation aperture, super-resolution, P-band

Citation Zeng T, Liu M K, Wang Y, et al. Tomographic SAR imaging with large elevation aperture: a P-band small UAV demonstration. Sci China Inf Sci, 2022, 65(3): 132303, https://doi.org/10.1007/s11432-021-3391-2

1 Introduction

Tomographic synthetic aperture radar (TomoSAR) implements an additional dimension of target discrimination by forming a second synthetic aperture in elevation [1–4]. By uniquely mapping a target in the real three-dimensional (3D) space to a position in the 3D imaging space, TomoSAR outperforms the traditional two-dimensional (2D) SAR by avoiding the problem of overlapping and foreshortening [5–7]. Unmanned aerial vehicle (UAV), especially, small UAV, is an appealing platform for airborne tomographic SAR imaging because of the advantages of rapid deployment and flexible trajectory planning [8,9]. Thus, small UAV based SAR tomography is a promising technique in aspects of urban 3D reconstruction, urban management, and critical situation detection [1,5,10–12].

Resolution is one of the most important performance indicators indicating the nearest distance that two adjacent targets can be discriminated. The elevation resolution TomoSAR can be expressed as

$$\rho_{sr} = \sigma \rho_s, \tag{1}$$

where ρ_s is the Reyleigh resolution and σ is the super-resolution factor.

The Rayleigh resolution is proportional to the length of elevation aperture [13]. The super-resolution factor is determined by the factors of SNR, the number of acquisitions, and target scattering features [14,15]. Provided a fixed super-resolution factor, the way to increase elevation resolution should be enlarging the length of elevation aperture. However, as the length of elevation aperture increases, the

* Corresponding author (email: yan_wang@bit.edu.cn)

geometric consistency of the image will deteriorate, i.e., the same target will be located at different relevant positions in different 2D images. For instance, two targets that overlap with each other will appear in different range-azimuth pixels in two different images. In this case, the image coregistration required by the traditional TomoSAR processing will fail. As a result, the traditional TomoSAR imaging method cannot be applied in a large elevation aperture case due to the problem of geometric inconsistency.

Aiming at solving this problem, this paper proposes a new super-resolution tomographic SAR imaging algorithm that can be applied for the case with a large elevation aperture. In principle, the new method gets rid of the necessity of 2D images coregistration by directly applying a 3D back projection like 3D grid-by-grid super-resolution imaging via compressive sensing (CS). Specifically, a 3D image space is firstly divided in the common illumination regions of all passes. Second, for each grid, the elevation signal vector is retrieved via interpolation in 2D images. Third, the achieved elevation signal is multiplied by a dechirping filter to locate the target at the grid, if any, to the zero-frequency position in the spatial spectrum. By judging the existence of the target using CS, target locations can be achieved. Finally, target amplitude and phase are inversed via the least square. The effectiveness of the method has been evaluated by both the computer simulations and real P-band small UAV TomoSAR experiments.

This paper is organized as follows. Section 2 analyzes the tomographic signal model and the geometric inconsistency problem with the large elevation aperture. Section 3 introduces the new super-resolution TomoSAR imaging method suitable for the large elevation aperture. The method is validated in Section 4 with both computer simulations and real P-band small UAV SAR data. The study is summarized in Section 5 with suggestions for possible future work.

2 Problem formation

2.1 Signal model

The geometric relationship of TomoSAR is shown in Figure 1. In this imaging geometry, x represents the flight direction of the platform (azimuth), r represents the direction of the line of sight and s is the elevation direction, which is perpendicular to the line of sight. The sampling in the elevation direction is represented by b, and Δb is the length of the elevation aperture. Thus, an elevation N-dimensional vector can be got, whose n-th generic element is given by [11,13,16]

$$h_n = \int_{\Delta s} \alpha(s) \exp\left(-\mathrm{j}\frac{4\pi}{\lambda} R_{b_n}(s)\right) \mathrm{d}s \quad (n = 1, 2, \ldots, N), \tag{2}$$

where $\alpha(s)$ represents the reflectivity function along elevation s, Δs is the elevation of the target, and $R_{b_n}(s)$ is the slant range history. According to Figure 1, the $R_{b_n}(s)$ can be obtained as

$$R_{b_n}(r, s) = \sqrt{r^2 - (s - b_n)^2} \approx r + \frac{(s - b_n)^2}{2r}. \tag{3}$$

2.2 Limit of traditional TomoSAR imaging

The elevation signal vector is retrieved from the same range-azimuth pixel of the registration image. After dechirping with the reference signal, the target elevation is estimated by spectrum recovery methods [17–21].

The method of the above process (first registration, then spectrum estimation) is a common process in current TomoSAR processing and has been widely validated in space-borne TomoSAR processing. However, in the space-borne TomoSAR analysis, due to the high orbital altitude and insignificant observation angle change, the migration caused by the elevation aperture can be neglected. In the case of UAV TomoSAR, a large elevation aperture is usually formed to obtain high elevation resolution. Hence, the migration history exceeds one range resolution unit, and the same target no longer appears in the same resolution unit of the repeat images. The migration constraint can be expressed as

$$R_1 - R_n < \rho_r \Rightarrow \frac{(s - b_1)^2}{2r_0} - \frac{(s - b_n)^2}{2r_0} < \rho_r \Rightarrow s < \frac{r_0 \rho_r}{\Delta b}, \tag{4}$$

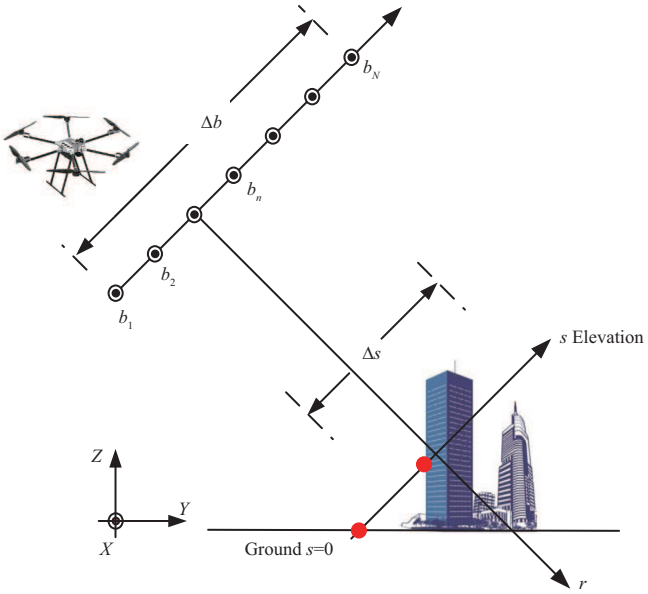

Figure 1 (Color online) Geometry of TomoSAR.

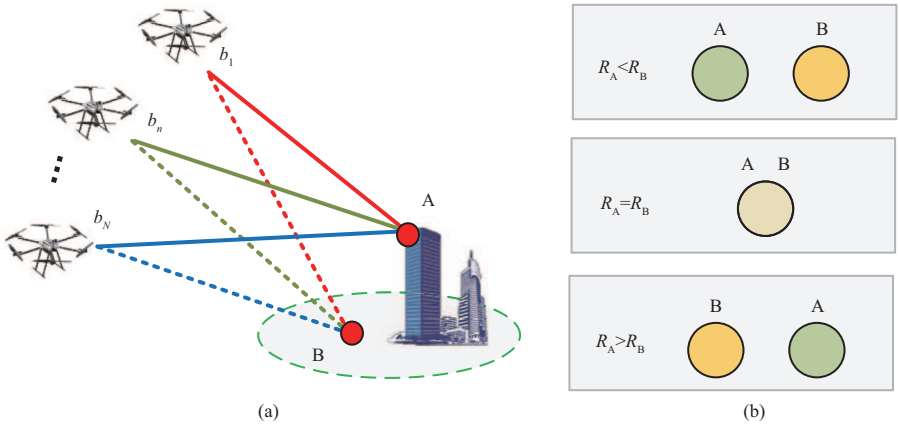

Figure 2 (Color online) The large elevation aperture UAV TomoSAR imaging schematic. (a) The geometry of repeat observations; (b) the imaging position change of A and B at the observation positions of b_1, b_n, and b_N. The slant range relationships corresponding to A and B exist for $R_{\rm A} > R_{\rm B}$, $R_{\rm A} = R_{\rm B}$, and $R_{\rm A} < R_{\rm B}$, respectively.

where R_1 and R_n are the range history of the target elevation s when the sampling position is b_1 and b_n, respectively. r_0 is the center range distance and ρ_r is the range resolution.

TomoSAR outperforms the traditional 2D SAR by avoiding the problem of overlapping and foreshortening. However, in UAV TomoSAR, the elevation migration history does not satisfy the condition of (4) due to the effect of the large elevation aperture. The same target will be located with different relevant positions. For instance, two targets that overlap with each other will appear in different range-azimuth pixels. In this case, the image coregistration required by traditional TomoSAR processing will fail. The large elevation aperture imaging schematic is shown in Figure 2. The UAV repeat passes form elevation aperture b_1 to b_N. At the sampling position b_n, the UAV to the scatterers A and B are at the same slant range and appear in the same azimuth-range pixel, as shown in the middle of Figure 2(b). However, due to the large elevation aperture, the migration caused by the target elevation is larger than that of the range resolution. The final result reacts as a separation of scatterers A and B, and even a crossover phenomenon, as shown in the top and bottom of Figure 2(b). As a result, the traditional TomoSAR imaging method cannot be applied in a large elevation aperture case due to the problem of geometric inconsistency.

Summarizing the occurrence of the above phenomena and problems, the definition of the large elevation aperture is as follows.

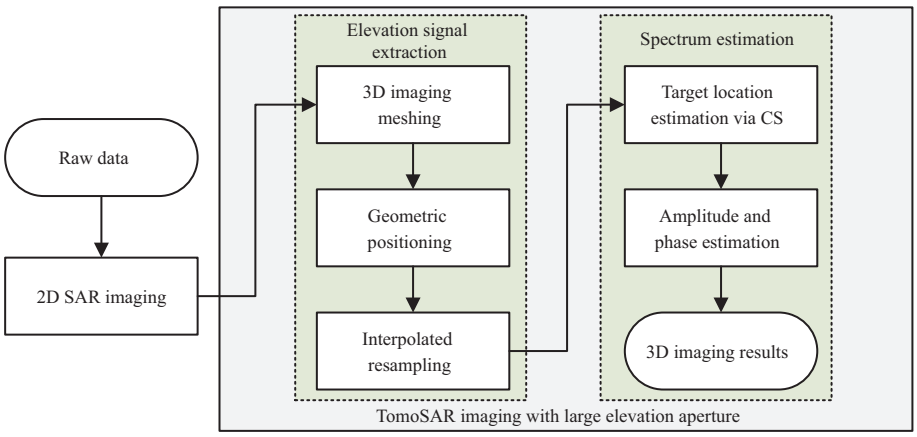

Figure 3 (Color online) Flowchart of the proposed approach.

(1) The migration caused by the elevation cannot be ignored, and the length of the elevation aperture does not satisfy the restriction of (4).

(2) The scatterers' intensity and phase information between images caused by the change of the observation viewpoint vary significantly, and the image decorrelation is obvious.

(3) In the worst case, the tomographic observation elevation aperture exceeds the critical baseline limit, and the image is noncoherent.

The elevation aperture that results in these situations can be referred to as large elevation aperture. In the case of the large elevation aperture, the image coregistration required by traditional TomoSAR processing will fail. As a result, the traditional TomoSAR imaging method cannot be applied in a large elevation aperture case due to the problem of geometric inconsistency.

3 TomoSAR imaging with large elevation aperture

In this section, a new super-resolution tomographic SAR imaging algorithm that can be applied for the case with the large elevation aperture is introduced. The new method performs CS imaging processing on a 3D imaging grid and hence avoids the necessity of 2D images registration. First, a 3D image space is divided into the common illumination regions. Second, for each grid, the elevation signal vector is retrieved via interpolation in 2D images. Third, the achieved elevation signal is multiplied by a dechirping filter to locate the target at the grid, if any, to the zero-frequency position in the spatial spectrum. A flowchart of the proposed approach is shown in Figure 3, and the details of some important steps are described as follows.

3.1 Elevation signal extraction

This subsection completes the extraction and vectorization of the elevation signal. The main steps include signal geometric localization and interpolated resampling.

First, the imaging geometry relationship between the scatterer and the imaging platform is used to achieve target localization. For the long elevation aperture, the extraction of elevation signal can be completed by equal range-Doppler equation, avoiding 2D images registration. The positioning and projection relationship is shown in Figure 4.

In Figure 4, P is the scatter, and P' is the position of the target P in the imaging plane. O is the azimuth position when the P point is irradiated on the broadside, O' is the position of O in the imaging plane. X is the velocity direction of the radar platform, Y is the range direction, and Z is the sky direction. From the principle of radar imaging, it is known that the projection P' and P should have the same slant range and Doppler in SAR imaging. Therefore, the slant range-Doppler equation shown in (5) can be combined to complete the solution of the position of $P'(x, y)$.

$$\begin{cases} |\overrightarrow{OP}| = |\overrightarrow{OP'}|, \\ f_d(\overrightarrow{OP}) = f_d(\overrightarrow{OP'}). \end{cases} \tag{5}$$

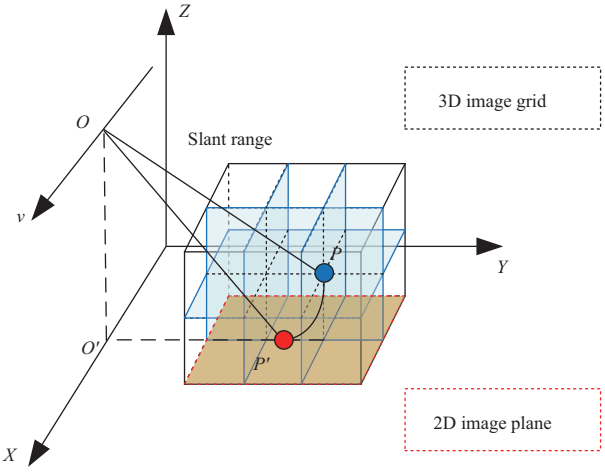

Figure 4 (Color online) The positioning relationship of the space target in the imaging plane.

In the broadside strip mode imaging, $f_{dc} = 0$, so that the Doppler surface can be considered as a plane passing OO' and P. OO' is perpendicular to the imaging plane. Suppose the coordinates of P $(P_{\rm A}, P_{\rm B}, P_{\rm C})$, then P' is

$$\begin{cases} x^2 - 2Ax + f(x)^2 - 2f(x)B = |\overrightarrow{OP}|^2 - P_{\rm A}^2 - P_{\rm B}^2 - P_{\rm C}^2, \\ f(x) = y = kx + b, \end{cases} \tag{6}$$

where $f(x)$ is the linear equation of $O'P'$ in the imaging plane, and the direction is the outer product of the normal vector of the imaging plane and the Doppler plane ($\boldsymbol{n}_L = \boldsymbol{n}_{\rm Im} \times \boldsymbol{n}_d$). Please refer to Appendix A for the derivation of $f(x)$. Finally, the relationship of the available coordinate x is shown in

$$\begin{aligned} &\left(1 + k^2\right) x^2 + 2(kb - P_{\rm A} - kP_{\rm B})x - {\rm Con} = 0, \\ &{\rm Con} = |\overrightarrow{OP}|^2 - P_{\rm A}^2 - P_{\rm B}^2 - P_{\rm C}^2 - b^2 + 2bP_{\rm B}. \end{aligned} \tag{7}$$

The solution of x as shown in (8), and the scatter imaging position can be obtained $P'(x, f(x))$.

$$x = \frac{-2(kb - P_{\rm A} - kP_{\rm B}) \pm \sqrt{4(kb - P_{\rm A} - kP_{\rm B})^2 - 4(1 + k^2){\rm Con}}}{2(1 + k^2)}. \tag{8}$$

After geometric positioning, the imaging position of P is precisely known, but it should be noted that usually this calculation often does not fall in the grid of 2D imaging. Therefore, in order to accurately obtain the image information of this coordinate position, the interpolation operation is needed. In this paper, bilinear interpolation is selected. In the above, the extraction of the elevation signal of the repeat passes is completed, and then the signal vectorization is constructed according to the elevation baseline distribution.

3.2 Target location estimation via compressive sensing

This subsection realizes the judgment of whether the interrogation point target exists. The main steps include grid-by-grid dechirping and the use of the CS algorithm to estimate the target spectrum.

First, the achieved elevation signal is multiplied by a dechirping filter to locate the target at the grid, if any, to the zero-frequency position in the spatial spectrum. By judging the existence of the target using CS, target locations can be achieved. The influence of the high-order phase is removed by dechirping, and the proposed approach constructs the reference signal grid-by-grid, so the residual high-order terms after dechirping processing are very small, and the more robust and accurate spectrum estimation results can be obtained.

The elevation signal model is shown in (2). The phase factor in (2) comprises a quadratic distortion (see (3)), due to the Fresnel or paraxial approximation. This distortion can be compensated by multiplying the reference signal. This step is often referred to as dechirping. The phase factor of the reference signal

always corresponds to the center elevation, also known as the zero reference position. The process is shown in

$$\begin{aligned} g_n &= h_n \exp\left[+\mathrm{j}\frac{4\pi}{\lambda}R_n(0)\right] \\ &= \int_{\Delta s} \alpha(s)\exp\left[-\mathrm{j}\frac{4\pi}{\lambda}\left(R_{b_n}(s)-R_{b_n}(0)\right)\right]\mathrm{d}s. \end{aligned} \tag{9}$$

After trivial manipulation,

$$g_n \approx \int_{\Delta s} \alpha(s)\exp\left[-\mathrm{j}\frac{4\pi}{\lambda}\frac{s^2}{2\left(r-b_{\|}\right)}\right]\cdot\exp\left[\mathrm{j}\frac{4\pi}{\lambda}\frac{b_{\perp n}s}{r-b_{\|}}\right]\mathrm{d}s, \tag{10}$$

where $b_{\|}$ is a parallel baseline, distributed along the radial direction, and $b_{\perp}$ is a vertical baseline, distributed along the elevation direction. In the past tomographic processing, the effect of constant phase (s^2) is usually neglected and considered as $r \gg b_{\|}$. The linear phase is retained and the tomographic signal phase is considered to be related to the elevation (s) only. However, the imprecision of the above assumptions can have an impact on the accuracy of the recovery and the subsequent application of the processing results. The effect of residual error is described in detail in [22].

But in the proposed approach, the tomographic signal is extracted by first selecting the spatial target and then localizing it according to the geometric relationship. In other words, for this tomographic signal, its corresponding elevation information is precisely known. Therefore, the accurate construction of the reference signal can be achieved based on the imaging grid, while there is no approximation and assumption in this construction process. Thus, there is no influence of residual phase and parallel baseline. When the spatial point corresponds to the presence of a target in the real scene, its corresponding signal model after dechirping is shown in

$$\begin{aligned} g_n &= h_n \exp\left[+\mathrm{j}\frac{4\pi}{\lambda}R_n(s_{\mathrm{ref}})\right] \\ &= \int_{\Delta s} \alpha(s)\exp\left[-\mathrm{j}\frac{4\pi}{\lambda}\left(R_{b_n}(s)-R_{b_n}(s_{\mathrm{ref}})\right)\right]\mathrm{d}s \\ &= \int_{\Delta s} \alpha(s)\exp\left[-\mathrm{j}\frac{4\pi}{\lambda}0\right]\mathrm{d}s. \end{aligned} \tag{11}$$

After the dechirping, a spectral estimation of the signal is required. The signal model after dechirping is discretized and can be written as shown in

$$\boldsymbol{g} = \boldsymbol{L}\alpha + \epsilon, \tag{12}$$

where $\boldsymbol{L}$ is the mapping matrix, $\boldsymbol{L}_{n\times l} = \exp(-\mathrm{j}2\pi\xi_n s_l)$. $\xi_n = -2b_n/\lambda r$ is the spatial frequency. Due to the sparsity of the elevation target, the spectral estimation problem of the tomographic signal can be transformed into the following CS problem:

$$\hat{\alpha} = \arg\min_{\alpha}\left\{\|\boldsymbol{g}-\boldsymbol{L}\alpha\|_2^2 + \|\alpha\|_1\right\}. \tag{13}$$

The solution to this problem can be processed with the help of CVX tools [23, 24].

According to the (11), when the target really exists ($s = s_{\mathrm{ref}}$), the peak of its signal spectrum should appear at the zero-frequency position. In other words, the achieved elevation signal is multiplied by a dechirping filter to locate the target at the grid, if any, to the zero-frequency position in the spatial spectrum. By judging the existence of the target using CS, target locations can be achieved.

3.3 Target amplitude and phase estimation

After estimating the target locations via CS, the mapping matrix $\boldsymbol{L}$ can be constructed accurately. The size of $\boldsymbol{L}$ is $N \times 1$, and the specific form is $\boldsymbol{L}_{N\times 1} = \exp(-\mathrm{j}2\pi\xi_n\hat{s})$. And the complex-valued reflectivity $\alpha(\hat{s})$ for this target can be obtained by solving the linear system equation, as shown in

$$\boldsymbol{g} = \boldsymbol{L}(\hat{s})\alpha(\hat{s}) + \epsilon, \tag{14}$$

Table 1 Key simulation parameters

Parameter	Value	Unit
Waveband	P	–
Bandwidth	60	MHz
Range	550–1000	m
PRF	≈ 52.08	Hz
Velocity	≈ 8	m/s
Height	170–260	m

where ϵ combines the measurement noise and the model error, for example, atmospheric phase error, deformation error, and baseline measurement error. Finally, the reflectivity of the target can be solved by the least square, as shown in

$$\hat{\alpha}(\hat{s}) = \left(\boldsymbol{L}^{\mathrm{H}}(\hat{s})\boldsymbol{L}(\hat{s})\right)^{-1}\boldsymbol{L}^{\mathrm{H}}(\hat{s})\boldsymbol{g}. \tag{15}$$

After the elevation signal extraction, target location estimation via CS, and target amplitude and phase estimation, the 3D imaging processing with a large elevation aperture can be completed. Through positioning (5), accurate dechirping (11) and estimation (13), and final amplitude and phase estimation (15), TomoSAR imaging with the large elevation aperture can provide robust and accurate 3D scattering estimation results.

The proposed approach is an extension of the traditional method and has a strong universality. In some special situations, such as a large elevation aperture, it shows better performance. It uses the "localization" to replace the traditional method of "registration" to achieve precise extraction of elevation signals. It can be said that the traditional method is a special feature of the proposed approach, and the elevation signal can be extracted by only using "registration". However, the method in this paper faces two problems. First, processing 3D grid points grid-by-grid, which consumes a lot of computing time. Second, the proposed approach relying on radar position information, when there is a motion error, the algorithm may be insufficient.

4 Experimental results

4.1 Computer simulation

This subsection shows the simulation experiments on the existence of problems with the large elevation aperture and the proposed method, respectively. The simulation parameters are listed in Table 1.

First, the simulation verifies that the overlapped target has a significant migration problem in the large elevation aperture tomographic observation because it does not satisfy the constraints of (4). The position of the two targets (x, y, z) are A $(700, 0, 30)$ m, B $(691, 0, 0)$ m, respectively. The tomographic sampling height is 170–260 m, the center height corresponds to a slant range of 716 m, and the corresponding height when the migration is negligible is 7.96 m. In order to better distinguish the two points, the amplitude of A is 1, and the amplitude of B is 0.6. The results for sampling heights 170, 215, and 260 m are shown in Figure 5.

From Figure 5(a), it can be seen that the migration with a large elevation aperture is significantly larger than a range resolution unit. The impact is reflected in the following: in the imaging results, the two points A and B have gone through the process of two independent points, overlapping, and independent again. It is worth noting that the relative positions of A and B are changed from A on the left side of B to A on the right side of B when they have separated again. This problem will lead to registration failure.

Then, a simulation of a 1D signal demonstrates the applicability of the algorithm with non-uniform sampling conditions. When the number of samples is relatively sufficient, the time-domain algorithm can be used to obtain the 3D imaging result with a large elevation aperture. However, the time-domain approach is severely constrained by the sampling locations. The performance of the time-domain algorithm is further deteriorated by the uneven distribution of elevation apertures while the elevation sampling itself is less. Figure 6 shows the comparison of the proposed approach with the time-domain algorithm in 1D signal processing. As can be seen in Figure 6, the truncated SVD method in the way of this paper has lower sidelobes compared to the time-domain algorithm, but the resolution is almost the same. However, in the proposed approach, the sidelobes are removed and the resolution performance is significantly

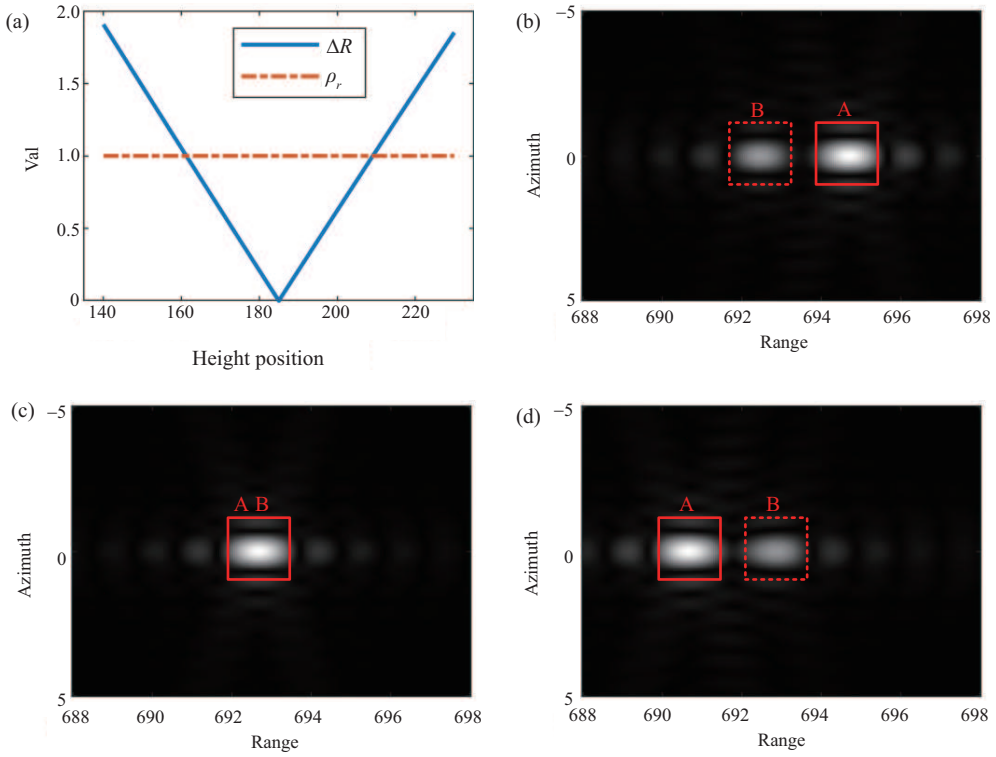

Figure 5 (Color online) Migration phenomenon caused by geometric inconsistencies with a large elevation aperture. (a) The slant range history difference of target points A and B is much higher than the range resolution (red dashed). In the imaging results at heights (b) 170 m, (c) 215 m, and (d) 260 m, point A and point B range from separation to coincidence and then to separation.

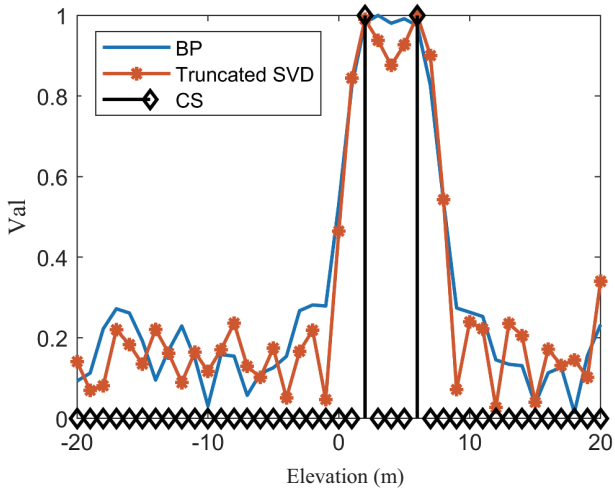

Figure 6 (Color online) Comparison of 1D signal recovery with a large elevation aperture. The blue line is achieved by the time domain algorithm, and the red and black lines are the results obtained from truncated SVD, CS recovery with the proposed approach, respectively. The distance between the targets in the simulation is 4 m.

improved. In this simulation, the resolution is set to 4 m, the target interval is 4 m, and the SNR is 10 dB.

To further verify the effectiveness of the proposed approach with a large elevation aperture, the simulation of the surface target is carried out. The elevation direction is sampled uniformly 30 times from 170 to 260 m. The simulation planes are shown in Figure 7(a), the height difference of the surface target is 30 m. The imaging results at 170 and 215 m are shown in Figures 7(b) and (c), respectively. It can be seen (in the red selected area) that the overlapped area is shifted due to the large elevation aperture. The scattering results have changed and there is a clear misalignment. Through the registration and

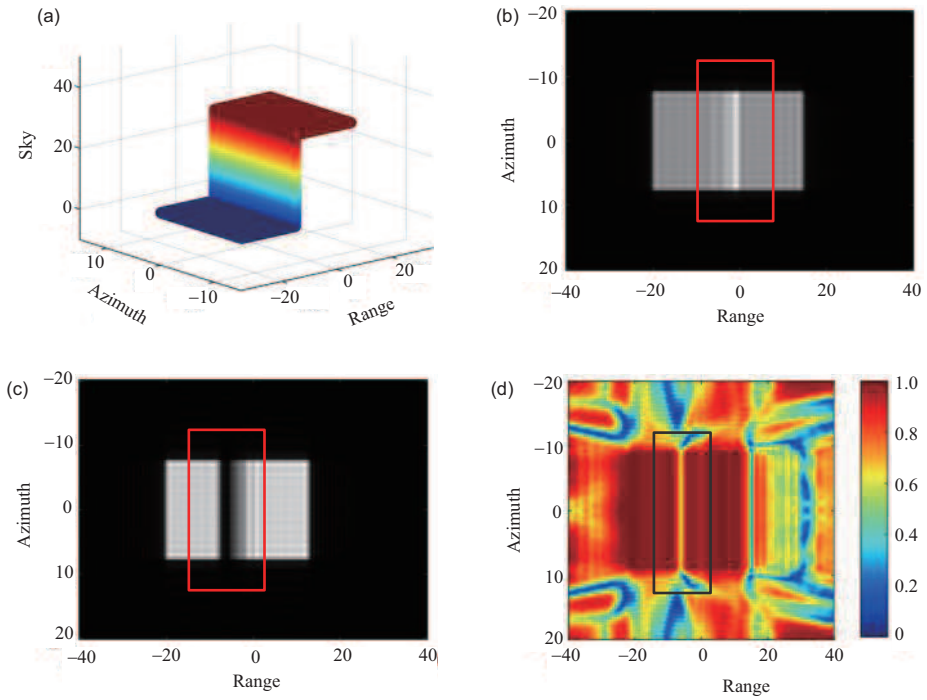

Figure 7 (Color online) Tomographic observation simulation on (a) surface target. The slave image with a sampling height at (b) 170 m, and the master image at (c) 215 m. The coherence map of (b) and (c) with a large elevation aperture is achieved by (d).

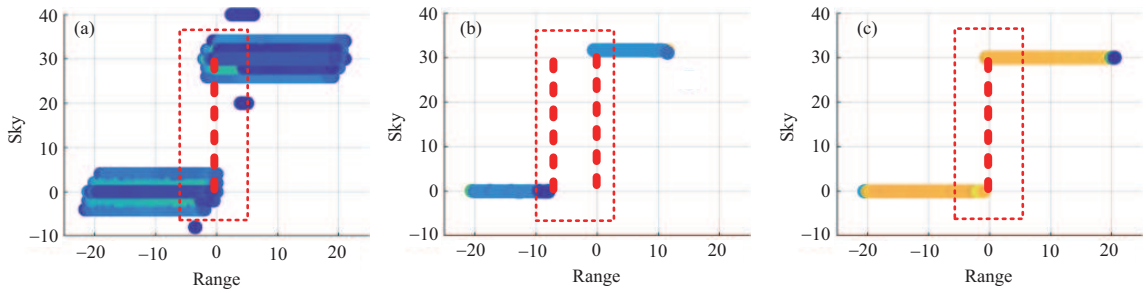

Figure 8 (Color online) Comparison of the 3D imaging results of the surface target by (a) BP, (b) the traditional method, and (c) the proposed approach with a large elevation aperture is shown. The red dashed line indicates the vertical extension direction of the estimated surface.

reprocessing of the elevation signal extracted from the same pixel, the overlapping target within the pixel changes. With the influence of this problem, it can be seen that the coherence decreases significantly in the middle region where the stacked mask is severely misaligned, as shown in Figure 7(d). This can lead to errors in elevation estimation.

The comparison 3D imaging results of BP (back propagation), the traditional method, and the proposed approach are shown in Figures 8(a)–(c), respectively. Since the simulated sampling is uniform, both the 3D BP and the proposed approach can recover the top and bottom positions of the building well. However, it can be seen that the resolution performance of BP is significantly poorer compared to the traditional method and the proposed approach. There is a significant spreading in the height dimension. Meanwhile, the traditional method based on registration processing cannot effectively recover the middle region due to the dislocation variation of overlapping targets with a large elevation aperture. As shown by the red dashed line in Figure 8(b), there is an obvious fault at ground position zero. In the traditional estimation results, there are obvious fracture results, and the endpoints of the upper and lower ground do not appear in the same position. However, the proposed approach can perfectly recover the target in the case of the large elevation aperture.

For the disappearance of the building facade structure in the estimated recovery, as shown by the red

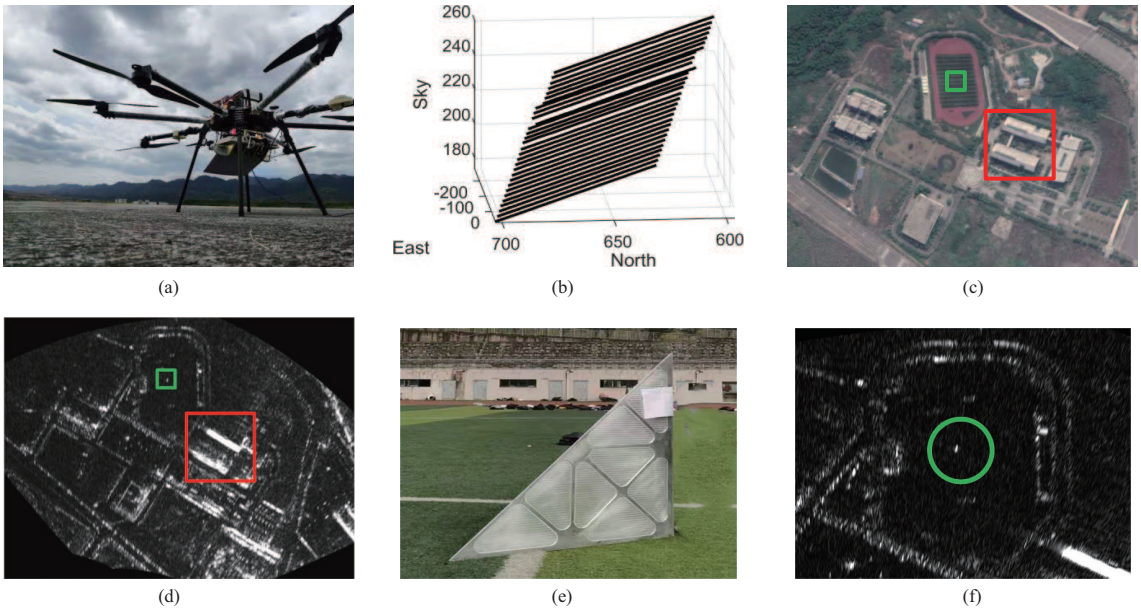

Figure 9 (Color online) The P-band experimental equipment and experimental scenes. The illuminated scene is Chongqing Aeronautical Institute. And a total of 30 sampling data with a 90 m elevation aperture are obtained. The green area is the location of the corner reflector, and the red area is the building. The above are the results of (a) multirotor UAV, (b) trajectory distribution, (c) optical map of scene, (d) SAR imaging result, (e) isolated angular reflector placed in the middle of the playground, and (f) SAR image of the reflector.

dashed line in Figure 8. For smooth walls, the main reason is the coherent superposition of electromagnetic waves on the wall, retaining only the top and bottom edge structure; for rough walls, its main reason is the small angle between the electromagnetic wave and the wall, resulting in weak backward scattering [25,26]. Therefore, it cannot be effectively recovered in its corresponding 3D image either.

4.2 Real P-band small UAV TomoSAR experiment

New UAV TomoSAR experiment data is successfully collected from Tonghang School, Chongqing, China, in March 2021. The small UAV TomoSAR system works in the P-band, and the corresponding parameters are listed in Table 1. The system is carried by a multirotor UAV and performed a total of 30 data acquisitions between 170–260 m altitude, the UAV and the flight trajectories are shown in Figures 9(a) and (b). The illuminated scenes mainly consist of areas from the campus, and the corresponding optical map and the SAR image are shown in Figures 9(c) and (d). The system incidence angle $\theta = 70^\circ$, the slant range from the center of the scene is 656.2 m, elevation aperture $\Delta b \approx 90$ m, which corresponds to an elevation resolution $\rho_s = 2.54$ m at this time. The red marked is the building area with more serious overlap, and the green area is the corner reflector placement area.

Figure 10 shows the interferogram at the large elevation aperture. Figures 10(a) and (c) are the interference and coherence results in the case of adjacent sampling, respectively. Figures 10(b) and (d) are the interference and coherence results when the distance from the master image is the farthest, respectively. It can be seen that the image coherence decreases severely under the large elevation aperture, and only some of the building areas retain well coherence. This is unfavorable to traditional methods.

A 1.1 m triangular reflector is arranged in the center area of the course as a target for the evaluation of the algorithm performance. The corner reflector and the corresponding SAR image are shown in Figures 9(e) and (f). The comparison shows the processing results of the BP algorithm, the traditional method, and the proposed approach, as shown in Figure 11.

The height estimation of the corner reflector is -8 m, and the estimation achieved by the three algorithms is basically the same. The presentation of 2D results is only selected for the reflector area normalized to an amplitude greater than -20 dB, so the presentation plots of the elevation results are not consistent across the algorithms. Compared with the BP algorithm, the traditional method and the proposed approach show significant super-resolution performance in the height direction. Since the corner reflector is flatly placed on the grass, there is no target and reflector hidden, and the traditional processing method based on registration is effective in this case. As can be seen from the reflector estimation results,

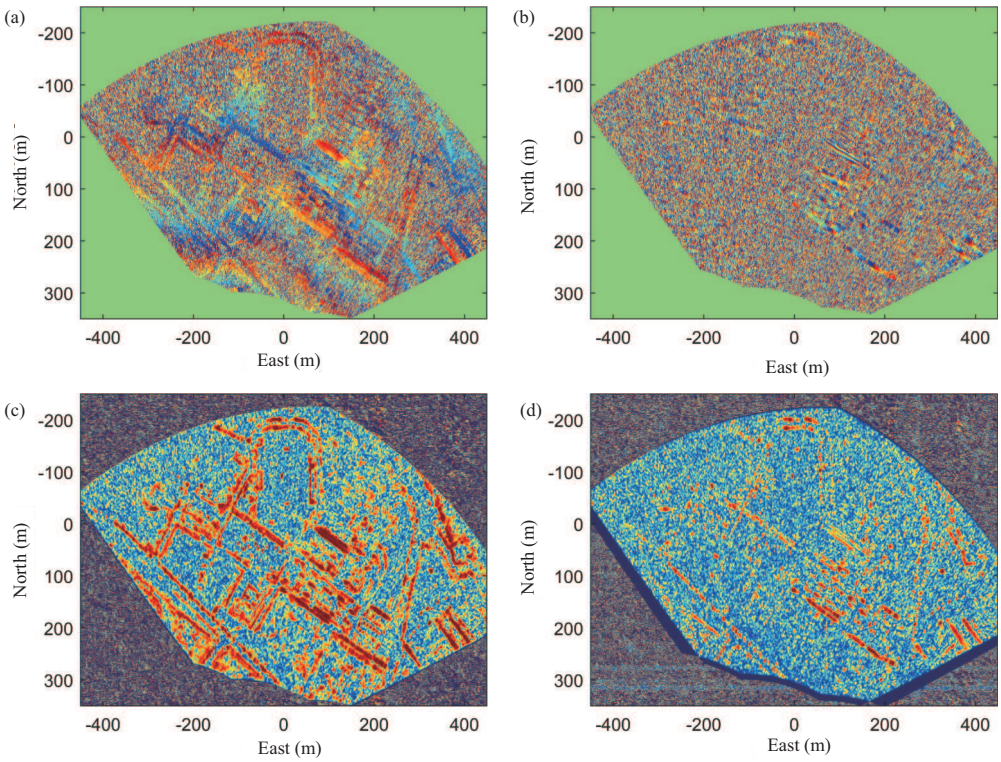

Figure 10 (Color online) The interferogram (a) and coherence map (c) between the acquisitions at 219 m and 216 m, respectively; and the interferogram (b) and coherence map (d) between the acquisitions at 219 m and 174 m, respectively.

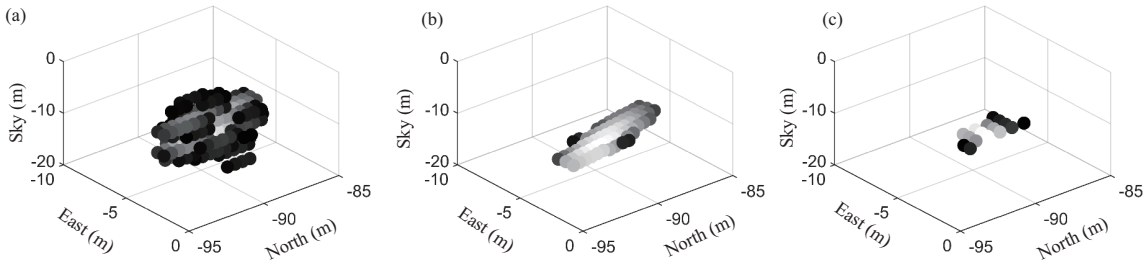

Figure 11 Comparison of the 3D imaging results of the corner reflector by (a) BP, (b) the traditional method, and (c) the proposed approach. Only the scattering points greater than −20 dB after normalization are selected.

the proposed approach is consistent with the conventional processing method without overlapping and cross-resolution unit migration. In the BP results, the height resolution is 2.62 m, PSLR (peak sidelobe ratio) is −14.01 dB, and ISLR (integral sidelobe ratio) is −10.32 dB. Due to the sparsity of the method in the recovery of height direction in this paper, its PSLR and ISLR cannot be effectively obtained, and the resolution evaluation result is 1.72 m due to the limitation in spatial search grid division. The traditional processing uses the same sparsity method (CS) to obtain only less discrete elevation estimation results within a range-azimuth cell, and cannot make an assessment of its resolution, PSLR, and ISLR.

Figure 12(a) shows the optical images of the observed buildings. Figures 12(b)–(d) show the imaging results for sampling heights at 219, 216, and 174 m, respectively. The results of Figure 12(b) are used as the reference master image. Corresponding Figures 12(b) and (c) are the imaging results of the closest and farthest from the master image, respectively. It can be seen from Figure 12 that with the influence of the large elevation aperture, the scattering of the building has changed significantly due to geometric inconsistencies, as shown in the red selected area in Figure 12. The overlapped target in the same resolution unit has changed, which will cause the registration result to be no longer valid. Thus, the extracted target after registration is no longer accurate, which will affect the elevation estimation result.

Figures 13(a) and (b) show the coherence maps after the registration process. The 219–216 m image pair is achieved by repeat passes images with the nearest distance, and the 219–174 m image pair is

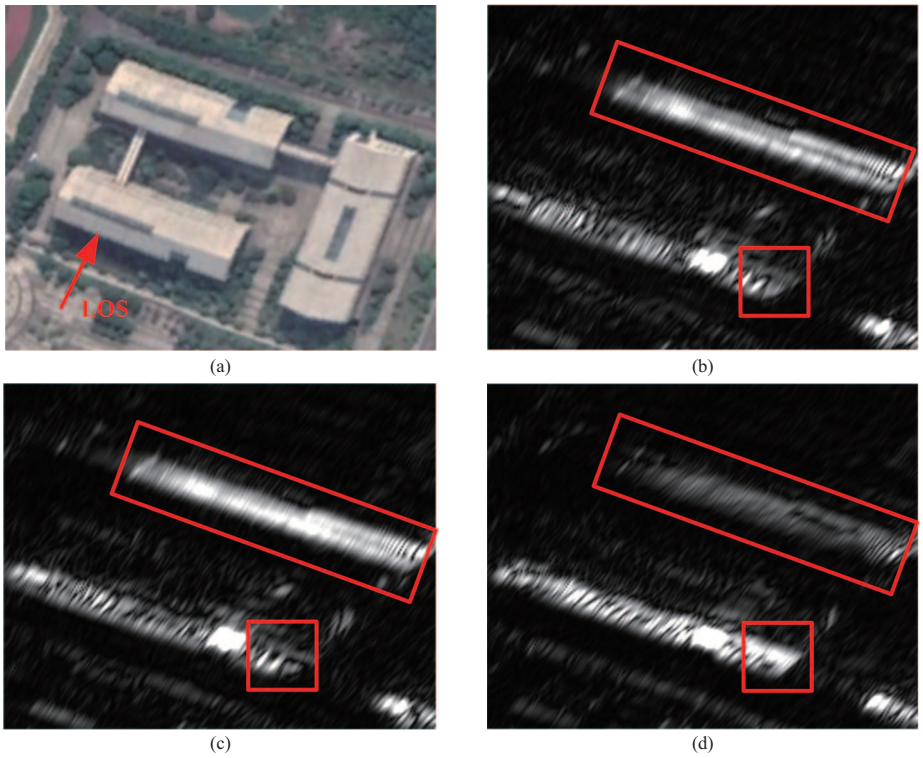

Figure 12 (Color online) Tomographic observation experiments on (a) building areas. The master image with a sampling height at (b) 219 m, and the slave image at (c) 216 m (nearest), and (d) 174 m (farthest).

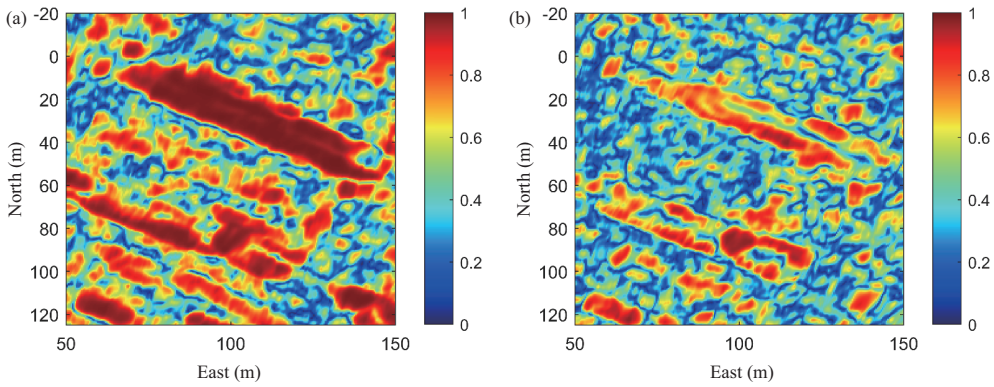

Figure 13 (Color online) Coherence maps between (a) Figures 12(b) and 12(c) and (b) Figures 12(b) and 12(d).

achieved by repeat passes images with the farthest distance. It can be seen that due to the influence of the large elevation aperture, the coherence of the data drops sharply, and the overlay information has obvious changes. In the set of coherence maps farther apart, the coherence deteriorates significantly and the building area coherence is no longer obvious. This will affect the processing quality of traditional methods. The comparison shows the processing results of the traditional method and the proposed approach, as shown in Figure 14.

The structure of the building facade in 2D imaging and 3D imaging exists disappearance phenomenon, and the simulation results are consistent with the performance, the specific causes and details refer to the literature [25,26]. The results are shown for all height estimation results after normalizing the magnitude for targets greater than -20 dB. From the results, it is clear that both methods can restore out the roof structure. However, in the traditional method, although the inclination of the roof part can be reflected, the target within the same resolution unit changes due to the influence of migration. This situation results in a large number of "noise points" in the estimation result, and the image quality is severely limited. In the proposed approach, due to the accuracy of signal search, the image noise is greatly reduced. The

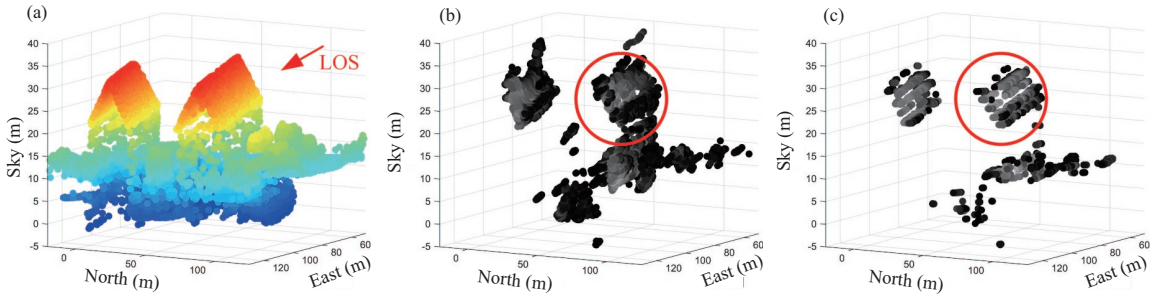

Figure 14 (Color online) Comparison of point cloud achieved by (a) LiDAR, (b) the traditional method, and (c) the proposed method.

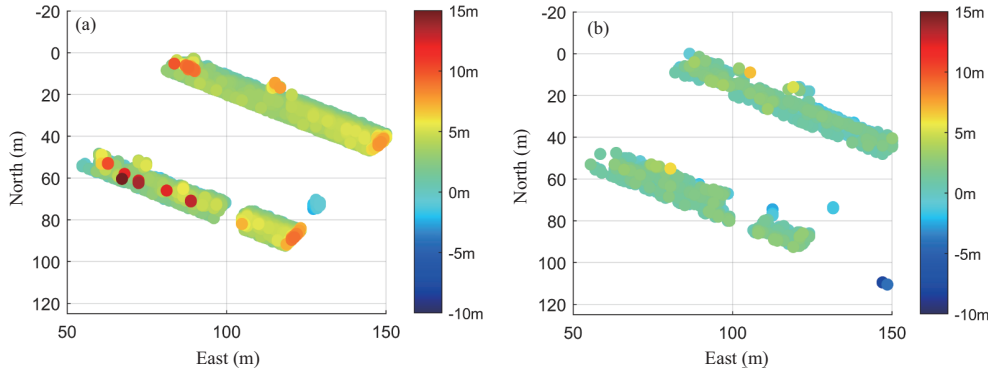

Figure 15 (Color online) Estimation error of the area in Figure 14 is achieved by comparing (a) the traditional method and (b) the proposed approach comparing to the LiDAR data.

estimation accuracy is significantly improved, and the slope change of the roof of the building is clearly shown. In contrast, the conventional method is 14.0796, and the proposed approach is 11.5432, which can be seen that the proposed approach has higher image quality. The estimation result is compared to the LiDAR data, and the estimation error is shown in Figure 15.

In order to facilitate comparison and display, Figures 15(a) and (b) use a consistent color quantization interval. According to statistical calculations, the mean of building height reversion error decreases from 1.8721 to 0.5698 m and the standard deviation of building height reversion error decreases from 1.8363 to 1.2023 m benefiting from the new approach. It can be seen that the proposed approach has more accurate and stable estimation results. Taken together, this paper can effectively solve the tomography imaging problem with a large elevation aperture and obtain high-quality 3D imaging results.

5 Conclusion

In this paper, a new super-resolution tomographic SAR imaging method has been proposed for the case with the large elevation aperture. Compared with the traditional method, the new one performs CS imaging processing on a 3D imaging grid and hence avoids the necessity of 2D images registration, which may cause geometric inconsistency. Specifically, the 3D imaging space is firstly created, followed by the interpolation based elevation signal extraction. Second, the dechirping processing is implemented grid-by-grid, followed by a CS processing to identify whether a target exists in the current grid. Finally, target amplitude and phase are estimated via least square based on the reversed target location. The proposed approach has been verified by both the computer simulations and real P-band UAV TomoSAR experiment, showing that the new one contributes to higher accuracy than the traditional method. Specifically, the mean of building height reversion error decreases from 1.8721 to 0.5698 m and the standard deviation of building height reversion error decreases from 1.8363 to 1.2023 m benefiting from the new approach. Future work may focus on applying the method in the case with higher frequency and higher resolution, as well as motion errors exist.

Acknowledgements This work was supported in part by National Science Fund for Distinguished Yong Scholars (Grant No. 61625103), in part by Beijing Natural Science Foundation (Grant No. 4202067), and in part by National Natural Science Foundation

of China (Grant Nos. 61971042, 61931002, 11833001).

References

1 Khoshnevis S A, Ghorshi S. A tutorial on tomographic synthetic aperture radar methods. SN Appl Sci, 2020, 2: 1–14
2 Li L H, Ding Z G, Wang Y, et al. Linear-array-MIMO SAR tomography: an autofocus approach for time-variant and 3-D space-variant motion errors. IEEE Trans Geosci Remote Sens, 2021. doi: 10.1109/TGRS.2021.3102072
3 Zhu Y T, Su Y. A type of M^2-transmitter N^2-receiver MIMO radar array and 3D imaging theory. Sci China Inf Sci, 2011, 54: 2147–2157
4 Reigber A, Moreira A. First demonstration of airborne SAR tomography using multibaseline L-band data. IEEE Trans Geosci Remote Sens, 2000, 38: 2142–2152
5 Rambour C, Denis L, Tupin F, et al. Introducing spatial regularization in SAR tomography reconstruction. IEEE Trans Geosci Remote Sens, 2019, 57: 8600–8617
6 Fornaro G, Lombardini F, Serafino F. Three-dimensional multipass SAR focusing: experiments with long-term spaceborne data. IEEE Trans Geosci Remote Sens, 2005, 43: 702–714
7 Zhu X X, Adam N, Brcic R, et al. Space-borne high resolution SAR tomography: experiments in urban environment using TS-X data. In: Proceedings of 2009 Joint Urban Remote Sensing Event, 2009. 1–8
8 Lort M, Aguasca A, Lopez-Martinez C, et al. Initial evaluation of SAR capabilities in UAV multicopter platforms. IEEE J Sel Top Appl Earth Obs Remote Sens, 2018, 11: 127–140
9 Ding Z G, Li L H, Wang Y, et al. An autofocus approach for UAV-based ultrawideband ultrawidebeam SAR data with frequency-dependent and 2-D space-variant motion errors. IEEE Trans Geosci Remote Sens, 2022, 60: 1–18
10 Chai H M, Lv X L, Yao J C, et al. Off-grid differential tomographic SAR and its application to railway monitoring. IEEE J Sel Top Appl Earth Obs Remote Sens, 2019, 12: 3999–4013
11 Zhu X X, Bamler R. Tomographic SAR inversion by L_1-norm regularization-the compressive sensing approach. IEEE Trans Geosci Remote Sens, 2010, 48: 3839–3846
12 Guillaso S, Reigber A. Polarimetric SAR tomography. In: Proceedings of POLINSAR'05, 2005
13 Fornaro G, Serafino F, Soldovieri F. Three-dimensional focusing with multipass SAR data. IEEE Trans Geosci Remote Sens, 2003, 41: 507–517
14 Liu M K, Ding Z G, Wang Y, et al. Analytic constraint between minimum number of acquisitions and SNR in SAR tomography. IEEE Geosci Remote Sens Lett, 2022, 19: 1–5
15 Zhu X X, Bamler R. Super-resolution power and robustness of compressive sensing for spectral estimation with application to spaceborne tomographic SAR. IEEE Trans Geosci Remote Sens, 2012, 50: 247–258
16 Budillon A, Evangelista A, Schirinzi G. Three-dimensional SAR focusing from multipass signals using compressive sampling. IEEE Trans Geosci Remote Sens, 2011, 49: 488–499
17 Stoica P, Moses R L. Spectral Analysis of Signals. Upper Saddle River: Prentice Hall, 2005
18 Gini F, Lombardini F. Multibaseline cross-track SAR interferometry: a signal processing perspective. IEEE Aerosp Electron Syst Mag, 2005, 20: 71–93
19 Capon J. High-resolution frequency-wavenumber spectrum analysis. Proc IEEE, 1969, 57: 1408–1418
20 Porfiri M, Ferro-Famil L, Nicolas J M. Building profile reconstruction using TerraSAR-X data time-series and tomographic techniques. In: Proceedings of the 8th International Workshop on the Analysis of Multitemporal Remote Sensing Images (Multi-Temp), 2015. 1–4
21 Reale D, Fornaro G, Pauciullo A, et al. Tomographic imaging and monitoring of buildings with very high resolution SAR data. IEEE Geosci Remote Sens Lett, 2011, 8: 661–665
22 Liu M K, Wang Y, Ding Z G, et al. High-resolution sar tomography via segmented dechirping. In: Proceedings of IEEE International Geoscience and Remote Sensing Symposium, 2020. 100–103
23 Grant M, Boyd S. CVX: Matlab software for disciplined convex programming, version 2.0 beta. 2013. http://cvxr.com/cvx/
24 Grant M, Boyd S. Graph implementations for nonsmooth convex programs. 2008. https://stanford.edu/~boyd/papers/pdf/graph_dcp.pdf
25 Franceschetti G, Iodice A, Riccio D, et al. SAR raw signal simulation for urban structures. IEEE Trans Geosci Remote Sens, 2003, 41: 1986–1995
26 Zeng T, Wei Y K, Ding Z G, et al. Parametric image reconstruction for edge recovery from synthetic aperture radar echoes. IEEE Trans Geosci Remote Sens, 2021, 59: 2155–2173

Appendix A Derivation of projection linear equation

$f(x)$ is the linear equation of $O'P'$ in the imaging plane. Assume that the height of the imaging plane is Z, and the normal vector of this plane is $\boldsymbol{n}_z$. The coordinates of radar is O, then its vertical foot in the imaging plane is O'. Then, the normal vector of the plane formed by the radar, the vertical foot and the target should be

$$\boldsymbol{n}_{\mathrm{RT}} = \frac{\overrightarrow{O'O} \times \overrightarrow{PO}}{\left|\overrightarrow{O'O} \times \overrightarrow{PO}\right|}. \tag{A1}$$

Then the direction vector of the radar-target in the projection plane (i.e., the projection $\overrightarrow{OP}$ of the $\overrightarrow{O'P'}$) is

$$\overrightarrow{D_{\mathrm{line}}} = \boldsymbol{n}_z \times \boldsymbol{n}_{\mathrm{RT}}. \tag{A2}$$

Then, it is possible to obtain

$$\begin{aligned} k &= D_{\mathrm{line}}\,(2)/D_{\mathrm{line}}\,(1), \\ b &= -D_{\mathrm{line}}\,(2)/D_{\mathrm{line}}\,(1) \cdot O'(1) + O'(2), \end{aligned} \tag{A3}$$

where '$*(1)$' denotes the x-coordinate of the point and '$*(2)$' denotes the y-coordinate of the point. The projection line equation can be obtained by bringing in the parameters

$$f(x) = kx + b. \tag{A4}$$